Programming Mechanical and Physicochemical Properties of 3D Hydrogel Cellular Microcultures via Direct Ink Writing

*Joselle M. McCracken, Adina Badea, Mikhail E. Kandel, A. Sydney Gladman, David J. Wetzel, Gabriel Popescu, Jennifer A. Lewis, and Ralph G. Nuzzo**

3D hydrogel scaffolds are widely used in cellular microcultures and tissue engineering. Using direct ink writing, microperiodic poly(2-hydroxyethyl-methacrylate) (pHEMA) scaffolds are created that are then printed, cured, and modified by absorbing 30 kDa protein poly-L-lysine (PLL) to render them biocompliant in model NIH/3T3 fibroblast and MC3T3-E1 preosteoblast cell cultures. Spatial light interference microscopy (SLIM) live cell imaging studies are carried out to quantify cellular motilities for each cell type, substrate, and surface treatment of interest. 3D scaffold mechanics is investigated using atomic force microscopy (AFM), while their absorption kinetics are determined by confocal fluorescence microscopy (CFM) for a series of hydrated hydrogel films prepared from prepolymers with different homopolymer-to-monomer (M_r) ratios. The observations reveal that the inks with higher M_r values yield relatively more open-mesh gels due to a lower degree of entanglement. The biocompatibility of printed hydrogel scaffolds can be controlled by both PLL content and hydrogel mesh properties.

1. Introduction

Hydrogel materials are exceptionally useful substrates for studying processes of cells grown in culture.[1] These materials can be patterned in three dimensions by myriad fabrication techniques, including electrospinning, electrohydrodynamic jet printing, micromolding, and stereolithography.[2] Alternately, hydrogel scaffolds can be produced by varying the solvent or cross-linker ratios in prepolymeric mixtures, yielding stochastically distributed scaffold porosity and compositionally sensitive modifications of mechanical properties.[3] Though useful for cellular cultures, these scaffolds lack well-controlled 3D spatial, geometric, and physicochemical cues that can be exploited to enhance cell migration, networking, elongation, and alignment.[4] Direct ink writing, an extrusion-based 3D printing method, provides a promising platform for the programmable fabrication of microperiodic scaffolds for applications in tissue engineering, in which extruded filament diameter, pitch, macroporosity, and material composition can each be independently controlled.[5] Optimization of ink rheology is crucial for the development of 3D printed scaffolds, requiring high viscosity, shear-thinning fluids that readily flow through small diameter printheads and exhibit shape retention after printing.[6] In an earlier report, poly(2-hydroxyethyl methacrylate) (pHEMA) inks were optimized for 3D printing by incorporating high-molecular-weight pHEMA chains, which served as a viscosifying agent, into prepolymer solution containing HEMA monomer that yielded smooth, fast-drying, UV-curable polymer filaments upon printing.[7] Tunable compositions of these pHEMA-HEMA (pHH) inks, coupled with well-defined architectures enabled by direct ink writing, provided an interesting route toward modulating hydrogel scaffold physicochemical properties and mechanics while preserving the macroporosity necessary for efficient nutrient/metabolite diffusion in cellular cultures.[8]

A central challenge to synthesizing complex 3D hydrogel scaffolds on which cellular behaviors and morphologies can be analyzed is the effective characterization of 3D scaffold materials' physicochemical properties. Confocal fluorescence microscopy (CFM) has been shown previously to be especially useful for imaging studies of pHH hydrogel scaffolds seeded with primary hippocampal neurons, and for characterizing the periodicity-dependent nature of their cellular responses to the scaffold geometry.[9] In the present study, CFM imaging methods are used to characterize how homopolymer additives influence both the hydrogel mesh properties and the chemical modification steps needed to afford robust activities for cell attachment and growth on the printed 3D scaffolds. To do so, microscale protein sorption kinetics were measured using

J. M. McCracken, A. Badea, D. J. Wetzel, Prof. R. G. Nuzzo
School of Chemical Sciences
University of Illinois Urbana-Champaign
Urbana, IL 61801, USA
E-mail: r-nuzzo@illinois.edu
M. E. Kandel, Prof. G. Popescu
Department of Electrical and Computer Engineering
University of Illinois Urbana-Champaign
Urbana, IL 61801, USA
A. S. Gladman, Prof. J. A. Lewis
Wyss Institute
School of Engineering and Applied Sciences
Harvard University
Cambridge, MA 02138, USA

DOI: 10.1002/adhm.201500888

Table 1. Mass fraction composition of pHH gels and solutions.

Type	Phase	Polymer	Curable components			Solvents			M_r
		pHEMA	HEMA	EGDMA	DMPA	dH_2O	EtGly	EtOH	
		[mass%]	78.5:2.5:1 mol ratio						
pHH-1	Film	8.00	49.56	2.40	1.24	18.80	10.00	10.00	0.15
	Gel	10.00	61.95	3.00	1.55	23.50	–	–	
pHH-2	Film	8.00	8.83	0.43	0.22	5.37	38.57	38.57	0.84
	Gel	35.00	38.65	1.88	0.97	23.50	–	–	
pHH-3	Film	8.00	3.40	0.16	0.08	3.58	42.35	42.35	2.19
	Gel	52.50	22.35	1.08	0.55	23.50	–	–	
pHH-4	Film	8.00	0.69	0.03	0.02	2.69	44.28	44.28	10.7
	Gel	70.00	6.05	0.29	0.15	23.50	–	–	
pHH-0	Film	8.00	9.10	0.22	0.11	5.37	38.6	38.6	0.85
	Gel	35.00	40.00	1.00	0.50	23.50	–	–	

arrays of pHH hydrogel thin films fabricated from inks with different polymer to monomer (M_r) ratios. **Table 1** lists the ink compositions used in this work, materials with M_r values chosen to bracket that of the original ink (pHH-0) used in prior studies of 3D neuronal cultures.[7] Correlated measurements using atomic force microscopy (AFM) are carried out to characterize the surface topographies of the films and the mechanics associated with adhesive interactions occurring at their surfaces.[10] These results are analyzed and compared in the context of cell growth activities evidenced in two classes of model 2D and 3D cellular microcultures carried out on scaffolds prepared using these materials.

The rigorous characterization of cellular responses to the pHH hydrogels is performed using a suite of imaging techniques that includes fluorescent assays on both living and fixed cell cultures, and, most notably, spatial light interference microscopy (SLIM), a long-term imaging modality for characterizing live cell dynamics that is at once label-free and quantitative. SLIM is a powerful imaging tool that combines principles of phase-contrast microscopy and holography to produce interferometric data capable of resolving quantitative features of subcellular dynamics. SLIM imaging has been previously used in numerous studies to measure motility, mass growth, or mass transport properties of numerous cell types.[11] In the present work, we combine the morphological and structural information derived from fluorescence assays with the cellular motility information afforded by SLIM imaging. We use these tools to describe a coherent narrative in which fibroblasts and preosteoblasts react to their environments in ways that, while cell line specific, are strongly impacted by the physicochemical attributes of the films and the modifications afforded by surface treatments that vary in nature as a consequence of differences in their underlying compositions.

The study reported here provides insights into features important for designing 3D scaffolds that can promote strong cellular viability — factors related to both the design rules of direct-write scaffolds and the physicochemical characteristics of the filaments used to construct them. Though pHEMA is a bio-inert polymer with low cytotoxic character, it does little to actively promote cellular attachment in model cultures.[12] The absorption of the cationic polymer ε-poly(lysine) (εPL) improves the biocompatibility of many material surfaces,[13] a form of chemical modification adopted in several of our studies of cells supported in microfluidic cultures.[14] In contrast to the effects engendered by nonspecific protein surface adsorption, in which cell function may be impeded by thickly accumulated proteinaceous layers, the absorption of εPL within a hydrogel substrate can be strongly activating and elicit improved attributes of biological compliance.[15] The current study shows that the compositional features of the pHEMA inks do impact the dynamics of an otherwise strongly preferential pHEMA–PLL interaction, with impacts on biological function.[16] These properties demonstrate a broader usefulness for application in the direct-write fabrication of bioactive 3D scaffolds that modulate kinetic attributes and the associated physicochemical features of protein sorption within the hydrogel material structures and the properties of cellular cultures in contact with them.

2. Results and Discussion

2.1. NIH/3T3 and MC-3T3-E1 Attachment and Growth on PLL-Treated Films

As noted in our earlier work, the attachment and subsequent development of cellular networks on 3D printed pHEMA–HEMA scaffolds (a composition herein referred to as pHH-0) requires a prior activating protein treatment to confer biocompatibility and facilitate on-filament growth.[7,17] The NIH/3T3 (3T3) and MC-3T3-E1 (E1) model cell cultures, examined here using four additional ink compositions that bracket the pHH-0 system, mirror the compositional sensitivities noted in that work. As expected, when pHH films are not treated with PLL, cells attach sparsely and generally migrate off (or fail to adhere to) the hydrogel, preferring to develop on the supporting glass substrate (S1, Supporting Information). We find that the compositional (M_r) differences in PLL-treated pHH films (Table 1 and described quantitatively in later sections) impact how both cell lines respond to the film scaffolds, and in specific cases improve their activities towards cell attachment and growth.

The results of Live/Dead assays of 3T3 and E1 cultures on PLL-treated and untreated pHH-2 films (a composition similar to the pHH-0 system and here compared against glass) are shown in **Figure 1**a,b after 24 h in culture. The pHH-2 film's performance, when compared to PLL-treated pHH-0 and other film composition types 1, 3, and 4, shows an improved biological compliance for the PLL-treated pHH-2 films. Even so, all PLL-treated films show more cell attachment and growth than their untreated (immersed in PBS only) counterparts, data for which are shown in detail in Figure S2 (Supporting Information). The degree to which PLL treatment enhances cell growth is different across 3T3 and E1 cell types, however, with E1 cells surviving well on untreated pHH-1 and pHH-2 film types, unlike 3T3 cells. There was no cell type, treatment, or length in culture tested that was found to induce even modest cell proliferation on pHH-3 and pHH-4 film types. Cell surface area coverage measurements from Live/Dead fluorescence assays in Figure 1c confirm the compositional dependence of the growth and attachment profiles found for 3T3 cells after 96 h in culture. Figure 1d shows the quantitative differences in live 3T3 and E1 cell surface area coverage after 24 h as well as those that emerge in 3T3 cells after 96 h in culture.

Rigorous statistical analyses of film type and treatment-specific properties across all data for each experimental condition show that both film properties and protein surface

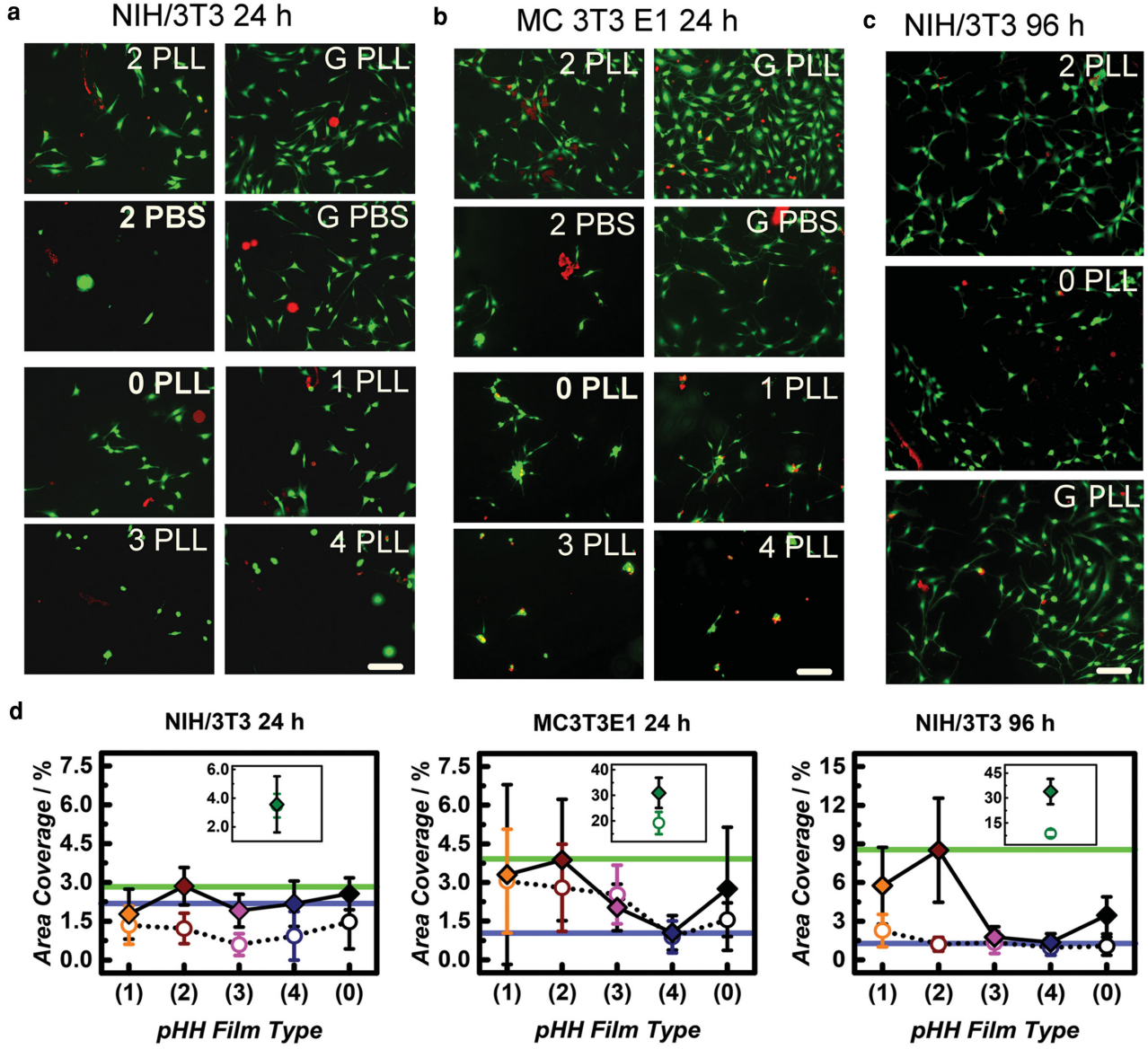

Figure 1. Live/Dead assays for NIH/3T3 (3T3) murine fibroblasts and MC3T3E1s (E1) murine preosteoblasts cultured on pHH film types 1–4, film type 0, and glass (G), that were either untreated (PBS) or treated (PLL) over the first days in culture. a) High growth compliance of 3T3 and b) E1 cell lines on treated and untreated glass and pHH-2 films after 24 h in culture and lower growth compliance of 3T3 and E1 cell lines on PLL-treated pHH film types 0, 1, 3, and 4, after 24 h in culture (scale bar 60 μm). c) Highest growth compliance substrates compared for PLL-treated pHH-2, pHH-0 films and PLL-treated glass for 3T3s after 96 h in culture (scale bar 50 μm). d) Cell coverage percentages are quantified for all film types for 3T3s (left) and E1s (center) after 24 h and 3T3s (right) after 96 h in culture with PLL treatment (filled markers) and without treatment (PBS, open markers).

treatment play significant roles in dictating cell growth outcomes. Within the context of an ANOVA analysis, individual film pairs (or groups) were specifically contrasted to verify their relative significance following a Box-Cox normalization of the data series and White's test for homoscedasticity. A complete description of the statistical methods used is given in S3 (Supporting Information). From this analysis, it follows that, for early time points (24 h) in the 3T3 fibroblast cell cultures, cell growth on PLL-treated pHH-2 and pHH-0 films is at or near the threshold for significance ($p < 0.05$). The relative significance for PLL-treated pHH-2 is increasingly revealed during longer culture intervals (96 h), with PLL-treated pHH-1 films showing growth compliance to a lesser extent, and pHH-0 lagging significantly behind these. A parallel growth compliance profile for (in decreasing order of growth compliance) pHH-2, pHH-1, and pHH-0 was observed for the E1 cell cultures, which were seen to emerge at earlier culture intervals (24 h) than for the 3T3 cells.

These data, when taken together with that given in S4 (Supporting Information), show confluence within the first week of growth, with healthy cell morphology, networking, and spreading consistently seen for pHH film compositions 0, 1, and 2 and generally reduced or inconsistent cell attachment and growth evidenced for pHH film types 3 and 4 (with stable cultures maintained for 2 weeks). These trends suggest that physicochemical features of the hydrogel, and perhaps the density of PLL presentation within it, the film mechanics, or a combination of these factors, must contribute to directly impact patterns of cell growth. We examine these features in the sections that follow.

2.2. Spatial Light Interference Microscopy Comparisons of 3T3 and E1 Motility

Substrate-dependent growth trends that are revealed by quantitative cell surface area coverage measurements generally overlapped between the two cell lines but did manifest some cell-specific differences. For example, while the pHH-2 film type is consistently the hydrogel most promotive of cell growth for 3T3 fibroblasts, a PLL treatment is essential for sustaining it robustly. For E1 preosteoblasts, this same treatment enhances growth but its absence does not proscribe it. As we show in the sections that follow, where we examine the morphological, structural, and motile differences that emerge in both cell lines' responses to 3D printed hydrogel scaffolds, the 3T3 cell networks develop on these materials in ways that are distinct from E1 cell networks.

To address the origin of the differences seen in cellular responses to the hydrogel films in a mechanistic way, we first compared representative images of live cellular morphologies of 3T3 fibroblast and E1 preosteoblast cells grown on treated and untreated pHH-2 films and glass (**Figure 2**a). Both 3T3 and E1 cell lines spread the most on the glass controls, as expected for comparisons made to cell spreading on soft, low modulus substrates. Of note are the comparable overall morphologies we observe for both cell types on PLL-treated pHH-2 films. On untreated pHH-2 films, the 3T3 fibroblast cells typically adhere poorly with a minimal surface area projection being noted. In comparison, the preosteoblast E1 cell morphologies seen on untreated pHH-2 films appear stunted, but still extend filopodia into their environments. These data demonstrate that the PLL treatment promotes attachment and growth for both cell types, albeit somewhat more beneficially for the 3T3 fibroblasts.

To examine the structural differences manifested in the cytoskeleton development between the cell lines on the gel substrates, we fluorescently stained the actin in each as cultured on the treated and untreated pHH-2, and glass controls (Figure 2b, with additional data for these and for less growth permissive substrates (pHH-4) given in S5, Supporting Information). We find that there is a dispersed, relatively weak, actin signal seen within the cytoplasm of 3T3 fibroblast cells on the treated pHH-2 film. The formation of actin bundles in 3T3 cells, typically along their periphery, develops in a more pronounced form in their culture on glass substrates. Pronounced actin bundles, by way of comparison, develop in a more evident way within E1 cells when they are cultured on both PLL-treated and untreated pHH-2 films (as well as on glass controls). We believe the robust actin cytoskeleton seen for E1 cells during their culture on pHH-2 films points to a higher E1 cellular motility relative to 3T3 cells, since the development of these structures is associated with cellular migration and therefore the effective cell-to-gel adhesion that facilitates that motion. The latter point is established more quantitatively in the sections below.

To address how physicochemical differences resulting from underlying film compositions affect cellular motility, we monitored 3T3 and E1 cell lines in real time over their first 96 h in culture with SLIM imaging. This information-rich method measures quantitative/mechanistic properties of cellular dynamics through an improvement brought to the traditional phase contrast microscopy.[18] The excerpted data shown in Figure 2c illustrates the nature of the motility seen for single, yet representative, 3T3 fibroblast and E1 preosteoblast type cells, here using data starting at 48 h and extending for up to 2 h more with images extracted as exemplars of larger, interval-frame-rate data sets. Qualitatively speaking, the E1 cells extend projections to as much as double the length as seen for similar motions of the 3T3 cells, and dynamically alter their cellular geometry at rates significantly exceeding similar processes of the 3T3 fibroblast cells. Representative high growth regions of PLL-treated pHH-2 films that were tracked from between 48 and 55 h in culture show a tendency for 3T3 cells to alternate within/between small clusters of cells, whereas E1 cells more often move independently with highly elongated but spreading morphologies being noted (Figure 2d, panel 1, 3). These data illustrate that the 3T3 and E1 cells respond to their hydrogel substrates in mechanistically distinctive ways that are likely driven by innate cell line properties and affinities.

We next specifically probed how cell-specific motilities are impacted by differences in the underlying physicochemical properties of the pHH films by tracking the cell motilities on PLL-treated pHH-4 films (Figure 2d, panel 2, 4) —a less growth-permissive material—and comparing motilities to those observed on PLL-treated pHH-2 films. The quantitative differences in cell motility for each of these cases were measured by tracking each cell present within the representative frame (Figure 2e), with cell motility values found to be significant in all cases except for 3T3 motility on pHH-2 films (Figure 2f), which was not significantly different from the reference 3T3 motility seen on the glass controls. Cells were also tracked on PLL-treated pHH-2, pHH-4,

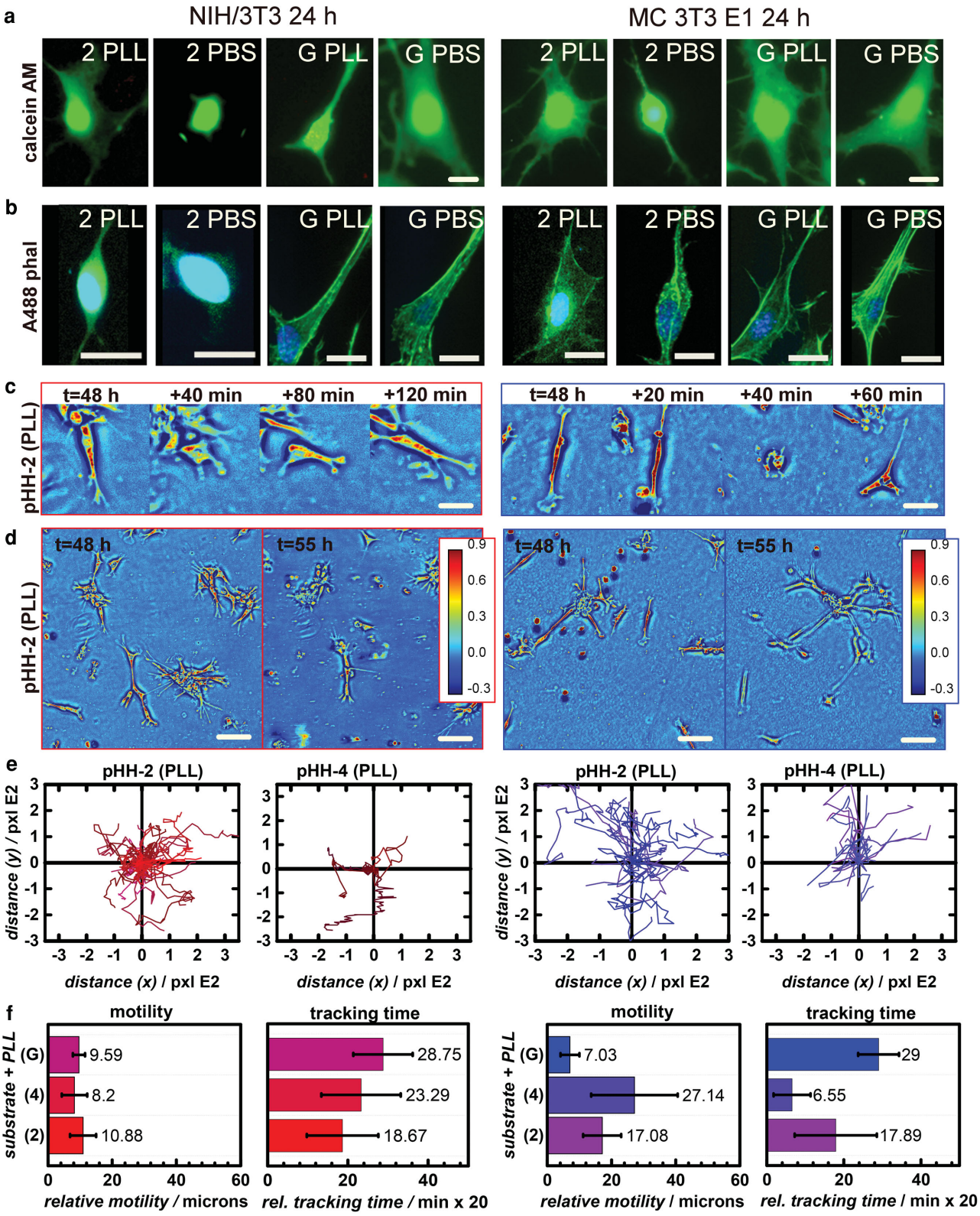

Figure 2. a) Individual calcein-AM-stained 3T3 and E1 cell morphologies on treated and untreated pHH-2 and glass substrates (scale bar 10 μm). b) Actin filaments of representative individual 3T3 and E1 cell morphologies on pHH-2 and glass after 72 h in culture (scale bar 20 μm). c) Spatial light interference microscopy (SLIM) tracking a single representative 3T3 (scale bar 20 μm) and E1 cell (scale bar 28 μm) over 2 and 1 h, respectively on PLL-treated pHH-2 films. d) SLIM tracking of representative regions in culture at 48 and 55 h for 3T3 and E1 cells on PLL-treated pHH-2 films (scale bar 100 μm) with e) relative motility data for 3T3 and E1 cell lines from 48 to 55 h in culture for PLL-treated pHH-2 and pHH-4 films. Scaling for cell motility plots is 1.59 pixel per μm. f) Quantification of relative motility and relative tracking time for E1 and 3T3 cells on PLL-treated pHH-2, pHH-4, and glass.

and glass substrates to monitor how long they remained within the field of view. From this analysis, we found that 3T3 cells on PLL-treated pHH-4 films were generally immobile (long tracking times). E1 cells on the same substrate were found to be generally transient (short tracking times), suggesting poorer attachment to their substrates.[19] The statistical analysis, as well as details of the tracking data, including studies on glass controls is given in S6 (Supporting Information). Additional excerpts of the SLIM data are given in S7 (Supporting Information) and the Movies S1–S2 (Supporting Information). For the 3T3 system on PLL-treated pHH-4 films, very few cells attached. Of those that did, there were insufficient nearby adhered cells to promote the formation of cellular networks, and the 3T3 fibroblasts generally remained immobile. Cooperative interactions between 3T3 cells are crucial for sustaining the relatively poor development of cells seen in these cultures. The surface area coverage of the E1 system on PLL-treated pHH-4 films were qualitatively similar, with — as before — very few cells attached. Of those that did, we saw more evidence of motile dynamics in which E1 cells would attach transiently, migrate, and more often detach again to appear as spherical live cell bodies lying at or near the film surface. Finally, we note that the results presented in later sections illustrate similar attachment and growth tendencies that are evidenced in 3D printed scaffold contexts as well. The substrate dependencies noted here — specifically the greater viability of the pHH-2 supported culture — are found to be strongly correlated with underlying physicochemical properties of the materials that serve to influence their PLL absorptive capacities and therefore the degree of PLL available for promoting cellular attachment. In the sections that follow, we examine this point in detail.

2.3. NIH/3T3 and MC-3T3-E1 Attachment and Growth on PLL-Treated 3D Scaffolds

We characterized cellular growth and attachment on 3D-printed scaffolds using the optimized pHH-2 material as a benchmark. These studies were carried out using an open-mesh scaffold comprising a four-layer pyramid printed as shown in **Figure 3**a, immersed in a PLL solution, seeded with 3T3 or E1 cells, and

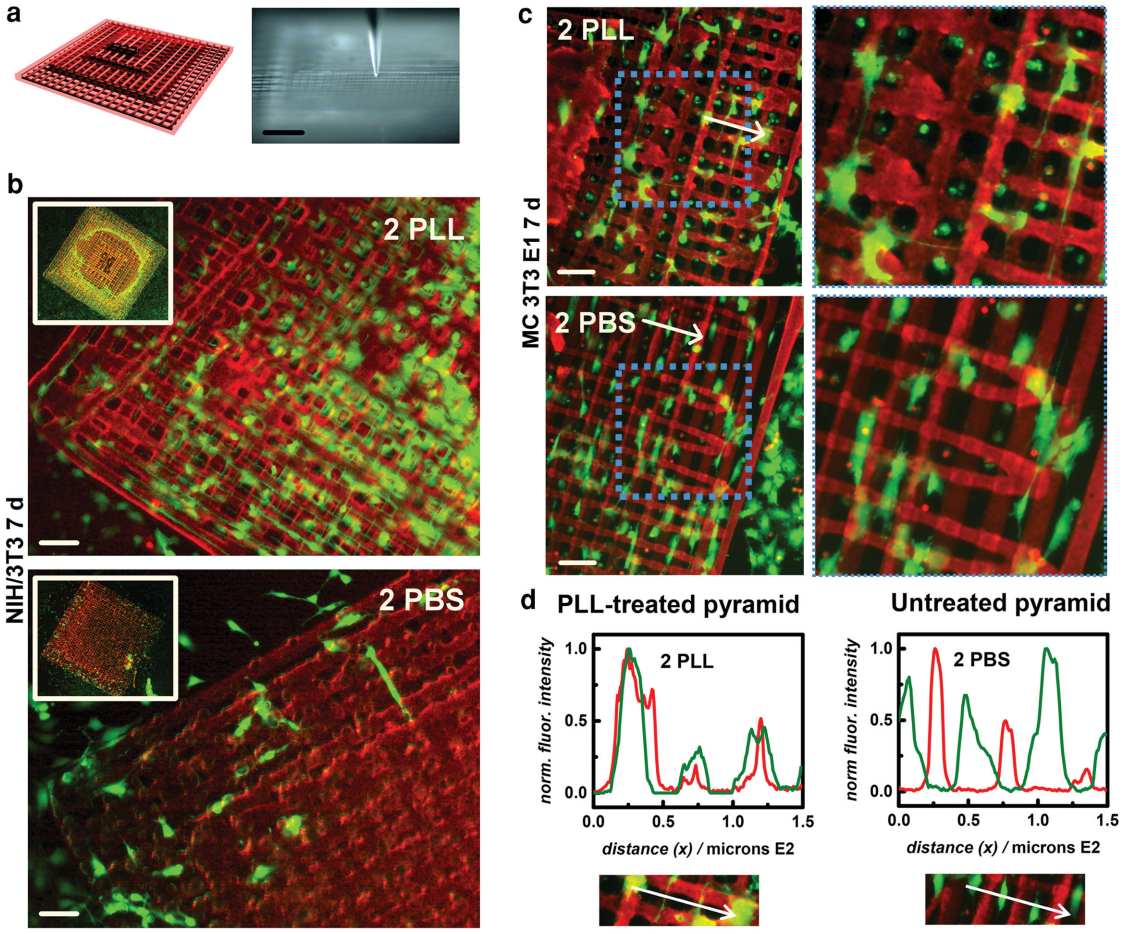

Figure 3. a) A 4 layer open-mesh pyramid (schematic on left) is 3D printed (right) with pHH-2 ink (scale bar 200 μm). b) Live/Dead assays show differences in on-scaffolds growth for 3T3 cells cultured on PLL-treated (top) and untreated (PBS) pHH-2 pyramids after 7 d in culture (scale bar 50 μm). c) E1 cells cultured on PLL-treated (top) and untreated (bottom) pyramids integrate onto scaffolds, with E1s on treated pyramids growing on scaffold filaments, and E1 cells on untreated pyramids growing adjacent to scaffold filaments (scale bar 100 μm). d) Line traces for representative image cross-sections show overlap of cell (green) and scaffold (red) fluorescence (PLL-treated, left) and alternation of cell and scaffold fluorescence (untreated, right).

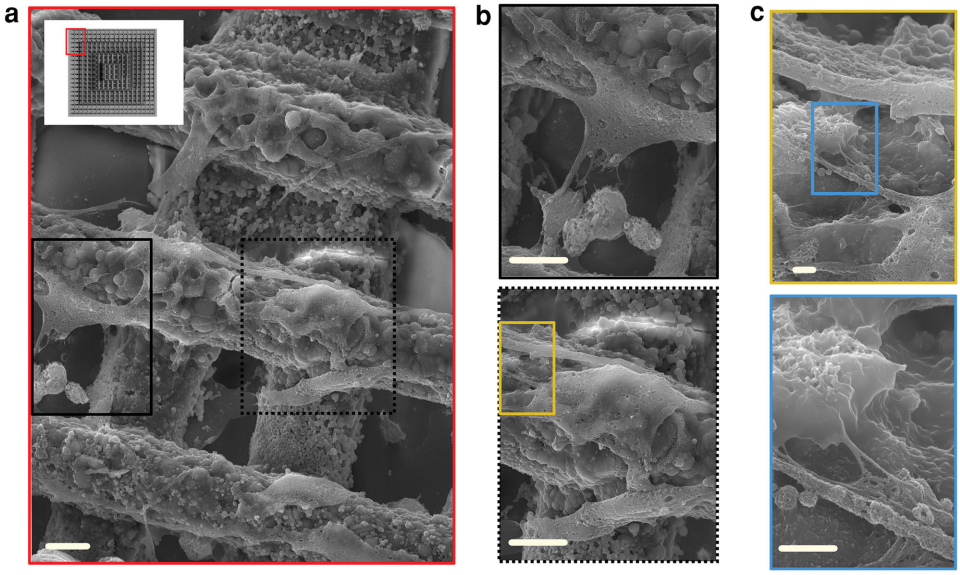

Figure 4. a) SEM imaging of 3T3 fibroblasts on a PLL-treated pHH-2 pyramidal scaffold (inset) with fibroblast spreading and on-filament growth and attachment (scale bar 10 μm). b) Fibroblast cells span gaps in the scaffold (top) to interconnect with neighboring cells and (bottom) filopodia project along the pHH-2 filament (scale bars 10 μm). c) Fine filopodia microstructure attach to pHH-2 microstructure (scale bars 1 μm).

maintained in culture for 7 d. Figure 3b (top) shows the robust on-scaffold 3T3 proliferation and spreading seen on a PLL-treated scaffold, a pattern that contrasts markedly with growth seen on an untreated scaffold (Figure 3b, bottom). Figure 3c shows a parallel trend in E1 cells seeded on the pyramid scaffolds and sustained in culture for 7 d, in which the E1 cells are found to attach and spread on scaffold filaments treated with PLL. The pattern of attachment and growth is very different on untreated scaffolds in this case. Here we see cells proximal to the scaffold fall to the supporting glass substrate, where they then align along the filaments. This tendency is directly compared for representative image cross-sections (line traces of which are shown as white arrows in Figure 3c) in Figure 3d where fluorescence signal distributions for both cells (green) and scaffold (red) are plotted for each case. The supported 3T3 cells visualized with scanning electron microscopy (SEM, which examines the morphologies of terminated cultures after dehydration) follows the trends in fluorescent studies, in which on-scaffold cellular growth is characterized by robust intercellular connections with morphologies that develop in close contact with the scaffold filaments (**Figure 4**a). The 3T3 cells are seen to frequently bridge filament gaps to interconnect with neighboring cells (Figure 4b, top) as well as to extend their filopodia in parallel to the long axes of the filament on which they are adhered (Figure 4b, bottom). The morphology of fine filopodia microstructure adhering to the underlying pHH hydrogel scaffold matrix is illustrated in the exemplary images given in Figure 4c. Additional SEM images are given in S8 (Supporting Information).

Due to geometric effects present in the open-mesh pyramid scaffold, a second type of pyramid was 3D printed with identical lateral dimensions except for the filament diameter, which was sufficiently large to eliminate open space between filaments. This yielded a gel pyramid several hundred microns in height, as shown schematically and during printing in **Figure 5**a. To illustrate the dynamical attributes of the PLL absorption, and the attendant formation of time-dependent infusive gradients, a cured pHH-2 pyramid scaffold was immersed in fluorescently-labeled PLL (FPLL) solution and the resulting spatial fluorescence distribution within it measured (Figure 5b). The temporal evolution of fluorescence intensity gradients is clearly evidenced throughout the scaffold, and with features of comparatively high surface-area to volume ratios (e.g., at the exterior vertices) exhibiting high fluorescence intensities. Detailed kinetics studies show that the quantitative details of the PLL-absorption within the gel change as the length of the incubation is increased. This feature is discussed in detail in the sections that follow.

A Live/Dead fluorescence assay performed on an untreated control scaffold (layer 1 of the pyramid) showed only a modest ingress and attachment of 3T3 cells after 7 d in culture (Figure 5c). For a PLL-treated scaffold, 3T3 on-scaffold growth is more advanced even after 4 d in culture, and by 18 d, 3T3 cell networks are apparent on every level of the PLL-treated pHH-2 pyramid including the apex as shown in Figure 5d. Additional images and supporting data for growth on other scaffold geometries are given in S9 (Supporting Information). Data from CFM imaging studies of the fibroblast growth (here fixed after 18 d in culture) conclusively establish that the 3T3 cells grow and in-fill on all tiers of the PLL-treated pHH 3D platforms, with representative data shown in Figure 5e for a pyramidal scaffold using fluorescently labeled nuclei to characterize axial (top) and lateral (bottom) fibroblast growth, respectively.

2.4. Composition (M_r) Dependence of FPLL Absorption by pHH Materials

To compare how compositional variations within a class of printable pHH ink affects the absorption of PLL into the

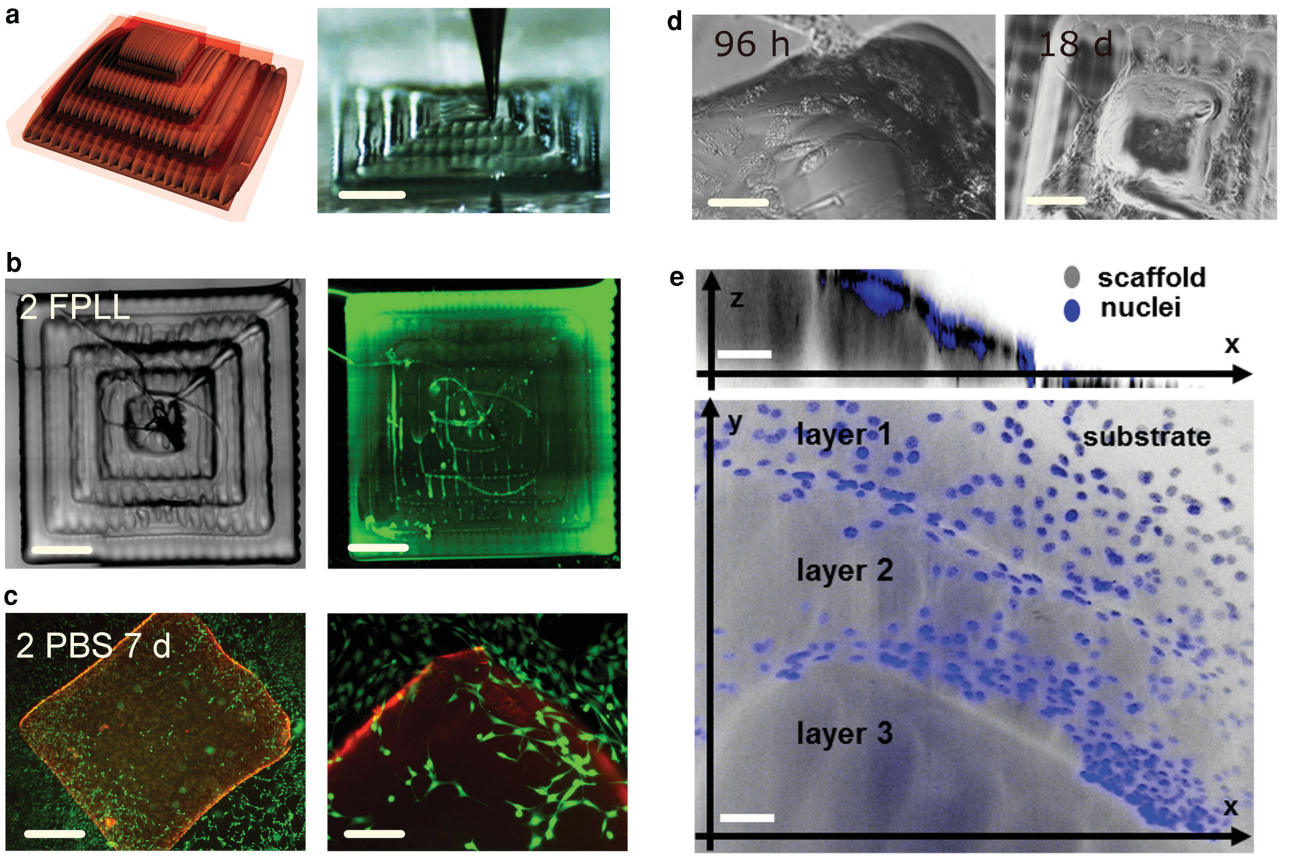

Figure 5. a) A four-layer closed-mesh gel pyramid (schematic on left) is 3D printed (right) with a pHH-2 ink. b) A light micrograph of the pyramid after curing (left) absorbs FPLL (right). c) LIVE/DEAD assays on an untreated closed-mesh gel scaffold (pyramid layer 1) allows for some 3T3 growth and attachment after 7 d in culture. d) Light images show robust on-scaffold growth for a PLL-treated pyramid after 96 h (left; scale bar) and 18 d (right; scale bar 150 μm). e) DAPI-stained nuclei of 3T3s grow over multiple layers of the pyramid scaffold (scale bar 60 μm).

hydrogel, pHH-0 and pHH-2 filaments and filament junctions were printed and incubated in FPLL. Representative post-incubation fluorescence micrographs for the two ink compositions are shown in **Figure 6**a. These data reveal that the equilibrium uptake of the FPLL is lower in the pHH-0 ink material. Extended quantitative analyses suggest an apparent relative equilibrium uptake of the absorbed FPLL in the ratio of approximately 2:5. Variances in filament dimensions of the pHH-0 and pHH-2 materials are too small to account for the intensity differences seen. This suggests that the matrix properties of the materials prepared from these chemically identical, but constitutively distinct, ink compositions directly impacts equilibrium protein absorption by them, a sensitivity examined in quantitative form in the sections that follow.

2.5. pHH Films from Rheologically Optimized Inks

To study the properties of the pHH materials, and the kinetics of PLL absorption into them, we prepared castable forms of the inks. The pHH-0 ink, a composition optimized for direct-write printing in an earlier study, was used here as a reference (and for which the rheological data are given in S10, Supporting Information). The range of M_r values selected for the cast series of pHH solutions was picked to bracket the compositional range of this optimized pHH-0 ink. To eliminate cross-linker effects on final hydrogel mesh properties, the relative mole ratios of HEMA:EGDMA:DMPA were kept constant across all pHH compositions. The mass ratio (M_r) used to distinguish these compositions is described by Equation (1):

$$M_r = \frac{m_{p1} + m_{p2}}{m_m + m_x} \quad (1)$$

where $m_{p1} + m_{p2}$ is the total homopolymer mass and $m_m + m_x$ is the total mass of HEMA monomer and EGDMA cross-linker incorporated into the prepolymer mixtures.

The range of M_r values examined here corresponds to a broad range of pHH materials properties that required the addition of the solvents ethylene glycol and ethanol to render them uniformly castable for cell growth and kinetics studies. Viscosities and densities of pHH solution compositions were compared in two cases: 1) with equal solvent mass fractions; and 2) with equal pHEMA mass fractions due to varied solvent additions. The data given in S11-12 (Supporting Information) comparing these properties confirm that equal pHEMA mass fractions of 0.08 yield pHH solutions that make highly uniform films upon spin-casting. After curing but prior to hydration, these

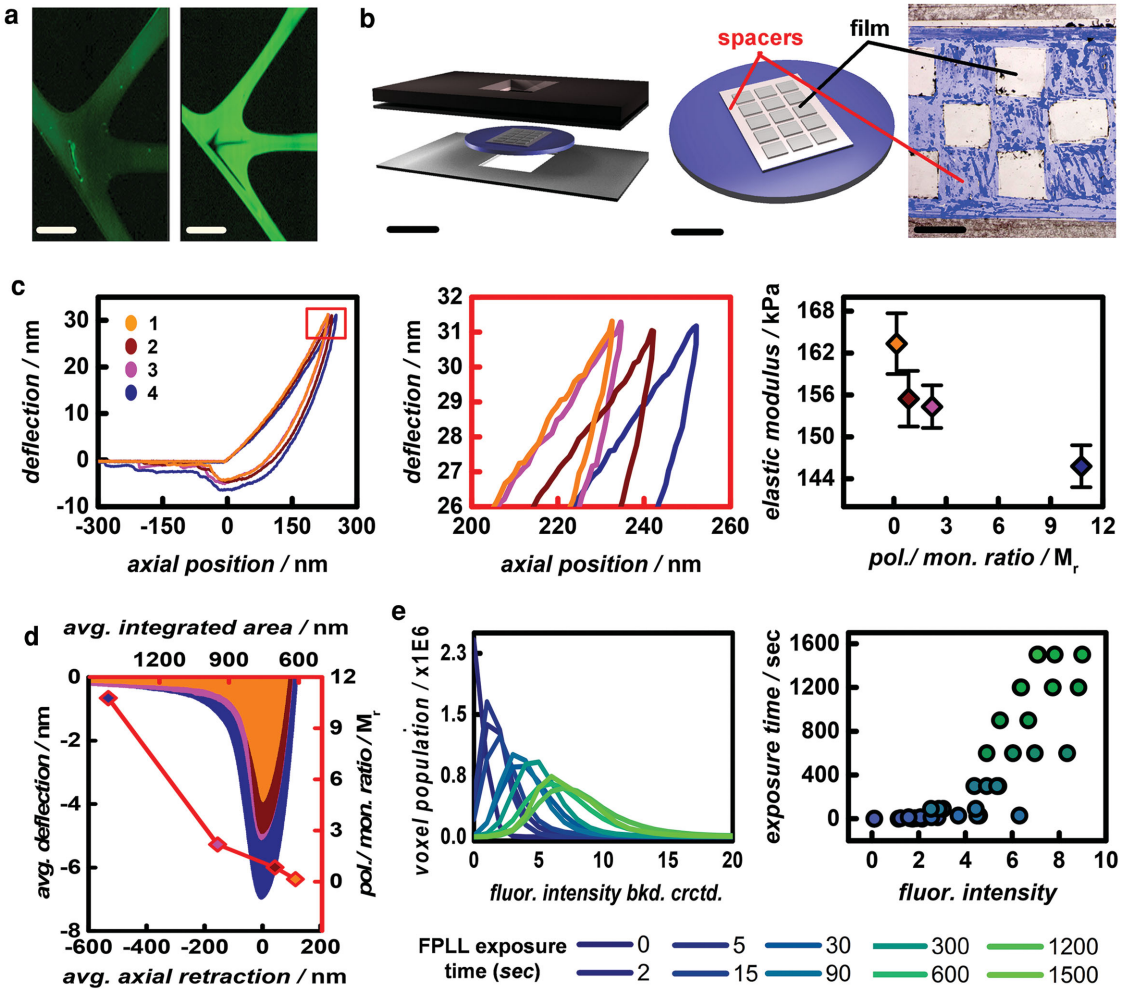

Figure 6. a) Relative fluorescence intensities for pHH-0 (left) and pHH-2 (right, enhanced equally for visualization, scale bar 50 μm). b) Microreaction chamber schematic for CFM kinetics experiments to measure composition-dependence of FPLL uptake by pHH film grids (left, scale bar 10 mm) with schematic (middle, scale bar 6 mm) and colorized thin-film pHH grid array (right, scale bar 2 mm). c) Single indent Hertzian AFM force curves for pHH 1–4 (left). Apex of indent force curves (middle). Elastic moduli from three 100-point force curves for pHH 1–4 (right). d) Average integrated adhesion areas for pHH 1–4. e) Single FPLL-uptake experiment background-corrected fluorescence intensity distributions from images taken for pHH-1 (left). Peak fluorescence intensities for all images and time points of a pHH-1 kinetic experiment (right).

glassy, optically clear films 1–4 had comparable thicknesses of ≈1.6 ± 0.1 μm (S13, Supporting Information). Exhaustive extraction of unreacted components into water over 72 h produced only minor reductions in the film thicknesses measured in the dehydrated state (S14, Supporting Information).

For the kinetics experiments, we selectively patterned the films, mounting them in a custom sample holder for CFM, as shown schematically in Figure 6b (left and middle), to allow a single film to be used within a kinetic experiment to minimize the effects of inter-sample variation. A micrograph of a representative film array, with its hydrophobic spacers, is shown in Figure 6b (right).

2.6. Mechanical Analysis of Thin-Film Substrates

Numerous studies have established that complex, and currently incompletely understood, relationships exist between cellular adhesion on scaffolds and the features of their underlying materials chemistry, especially the spatial presentation of adhesion-promotive proteins (of which PLL is one example), as well as the role that material mechanics serve in affecting cellular behaviors.[20] For this reason, we first carried out AFM studies of the films described above to quantify the mechanical properties of the various composition pHH materials. Deflection curves generated from AFM indentation experiments were converted to force curves using the relationship given in Equation (2):

$$F_n = k_c(d - d_1) \quad (2)$$

which relates the normal force F_n applied at the surface to the cantilever spring constant, k_c, and the deflection, d, where d_1 corresponds to the zero-deflection position of the cantilever.

The experimental force curves were analyzed using a Hertzian model commonly applied to AFM indentation data for elastic, non-adhesive materials including gels.[21] Controls,

based on an extensive analyses of replicate measurements, showed adhesive interactions were statistically negligible (shown in S15, Supporting Information).[22] Representative force curve data for a single indent of each film type are given in Figure 6c (left), with the axes expanded to illustrate the subtle differences seen between the film types (middle). Fits of the AFM indentation data were made on 100-indent force maps taken in three discrete areas for each pHH film type using the generalized force-indentation Equation (3):

$$F = \lambda \delta^{\beta} \tag{3}$$

where F is the force applied to the indenter, δ is the indentation depth, and λ and β are quantities dependent on indentation tip geometry.[23] A detailed discussion of the force measurement methods and indentation depth parameters (as well as approximations used for the mechanical analyses) is given in S16 (Supporting Information). The parameters of note in this analysis include the Poisson's ratio for the indenter tip ν_i (0.25), the contact area radius R (assigned an approximate value of 100 nm), and the reduced elastic modulus, E_r. Taken together these parameters can be used to calculate the sample's elastic modulus using Equation (4):

$$\frac{1}{E_r} = \frac{(1-\nu_i^2)}{E_i} + \frac{(1-\nu_s^2)}{E_s} \tag{4}$$

where E_i and E_s are the elastic moduli for the indentation tip and the sample, respectively, and $\nu_s = 0.29$ is the pHEMA Poisson's ratio reported in the literature.[24] The results for the pHH hydrogel thin film series shown in Figure 6c (right) yielded quantitative values for the film elastic moduli, with the highest elastic modulus observed for pHH-1 and the lowest elastic modulus for pHH-4. Film types 2 and 3 exhibited mechanical properties bounded by these limiting values.

Optimal environments for cellular adhesion require a balance between migration and attachment, so that cells flatten onto their substrates but are not bound such that they form islands or fail to network with neighboring cells.[25] A separate adhesion analysis was performed to study this property from the retraction portion of the AFM force curves, due to the considerable depth and contribution of adhesion for this section of the mean force curves. Our aim was to determine what, if any, role surface energies may have in biocompliance outcomes. The average adhesion well depth calculated from the mean deflection distance for all axial points on the retraction curves (n = 300 per film type) was found to increase in order from pHH type 1 to type 4 films, with pHH film types 2 and 3 again exhibiting intermediate behaviors. The adhesion force illustrated a complementary trend, one in which an increase in adhesion corresponded to a decreasing elastic modulus. The integrated area of the average adhesion curve for each material type was determined and plotted against the pHEMA mass fraction of the corresponding film, the results of which are presented in Figure 6d. Though the axial indentation depth was approximately constant for all force curves, the proportional scaling of the adhesion forces for these films lead us to conclude that higher degrees of adhesion were associated primarily with indent geometry differences due to the deformation of the lower elastic modulus materials and not from fundamental changes in the hydrogel surface energies. We finally note that many of the individual adhesion curves exhibited complex profiles that may reflect dynamics involving decohesive bonding upon retraction (S17, Supporting Information).[26] These dynamical attributes appeared to be much more pronounced (and common) for the pHH-4 films — those with the highest pHEMA mass fraction and the lowest number of structural crosslinks. From these analyses, we find it unlikely that differences in cellular growth and attachment across pHH film types originate from surface energy differences, but instead from the variable presentation of absorbed PLL that in fact renders the pHH films biocompliant.

2.7. Quantitative Analyses of PLL Absorption Dynamics in pHH Gels

As noted above, qualitative observations establish a temporal sensitivity for the uptake of PLL by the various pHH gels. We carried out detailed measurements using thin-film substrates and FPLL to better quantify the dynamics involved. The substrates used in these experiments are sufficiently thin to allow rapid removal of non-bound FPLL upon rinsing the films prior to imaging, allowing a direct measurement of the total quantity of strongly absorbed FPLL. The data do not fully resolve the axial distribution of the fluorescence intensity present in the pHH thin-film materials. For this reason, the spatial gradients inherent to FPLL diffusion into and absorption within the hydrogel matrix were not characterized directly with this experiment, but their possible contributions to overall fluorescence measurements were carefully considered and excluded (S18, Supporting Information). An apparent diffusion coefficient for the temporal evolution of a PLL gradient can be calculated, however, based on measurements of intensity in accordance with a model with several simplifying assumptions. First, we assume that the absorption of the PLL by the pHH involves multi-segmental interactions and is essentially irreversible in nature. Second, the absorption of the PLL in specific regions inhibits/precludes additional adsorption of the protein in those same regions. Third, the effective sticking probability for this massive molecule in an open region is likely to be very large (here we assume unity). Finally, as the sample is incubated, uptake is assumed to be fastest at the ambient solution interface of the gel and increments as the PLL penetrates deeper into the pHH matrix. Since time-dependent uptake of FPLL corresponds to the equilibrated absorption of FPLL throughout the entire film, the temporal absorption gradient so engendered will only be seen (and best quantified) by integration through the entire z-depth profile (more information regarding the development of metrics for CFM optical stack analyses is given in S19 (Supporting Information). We therefore used the mean maximum fluorescence intensity (MMFI) to quantify the FPLL-exposure time-dependent changes in protein uptake by the gel. By extracting only the maximum voxel intensity from an entire axial stack, the MMFI emphasizes trends tracking the relative increase in average PLL composition as effected over the course of a single kinetic experiment. Exemplary data for temporal distributions of voxel intensities measured from confocal

images within a single pHH-1 kinetic experiment are given in Figure 6e (left). The general trends show a marked broadening of the fluorescence intensity distributions occurs with increasing FPLL exposure time. The data in Figure 6e (right) plots the corresponding average maximum intensities for this experiment as are calculated from the fluorescence intensities of the peak voxel population for each voxel intensity distribution curve. These data are part of a broad set of replicate experiments that show that the integrated intensities increase markedly with time. A more detailed discussion of mass transport in relation to this measurement and data for other film types is given in S20 (Supporting Information).[27]

2.8. Modeling FPLL Absorption Kinetics

The suitability of several physical and semi-empirical models to fit the experimental data described above was tested. These include integrated kinetic functions reported in the literature following pseudo-first order (PFO), pseudo-second order (PSO), and biphasic models. Aspects of the underlying physical assumptions of these models (given in S21, Supporting Information) mitigate against their consideration.[28] As embedded in the dynamical assumptions discussed above, we found that Fickian models of diffusion kinetics present both superior mathematical fits and more plausible physical interpretations for this materials system. Modeling diffusion in polymeric film systems has been studied extensively in the literature, with a number of different models used to describe instances of deviation from classical Fickian behaviors.[29] According to Fick's second law, a simple power law equation described for generalized diffusional solute uptake behavior in polymeric systems is given by Equation (5):

$$\frac{M_t}{M_\infty} = kt^n \tag{5}$$

where M_t/M_∞ is the fractional value of mass uptake at time t over mass uptake at times approaching infinity, k is a constant incorporating characteristics of the macromolecular network, and n is a diffusional exponent coefficient indicative of the transport mechanism.[30] For ideal Fickian diffusion, n values of 0.5 for a slab geometry (and lower values down to 0.43 for geometries presenting with varying aspect ratios) are expected. When heterogeneity in the polymer film is present, more complex scalings are expected and generally found.[31]

For the present data, we considered a modified version of the generalized diffusion equation as the basis for the analysis of CFM data, one that assumed a linear correlation between a mass transfer-limited change in composition and fluorescence intensity such as is given in Equation (6):

$$M_t = bF_t \tag{6}$$

where b is a coefficient relating fluorescence intensity per voxel to fluorescently labeled protein mass, and F_t is the fluorescence intensity measured at exposure time t. Use of a diffusional change in mass fraction in the generalized diffusion equation permitted direct application of Equation (5) in modified form as given in Equation (7):

$$\frac{F_t}{F_\infty} = kt^n \tag{7}$$

where F_t/F_∞ is the fractional value of mean total fluorescence intensity (MTFI) imaged for a given film volume over the MTFI at the maximum value calculated for a near-equilibrium time point. As discussed in the Supporting Information, the MTFI values represent one of several methods of assessing the composite data such as those presented in Figure 6e. Correlation coefficients of $0.950 < RSQ < 0.968$ for curve fits using Equation (8) across the film series were calculated for the entire kinetic curve for each pHH film type. The quality of these fits, which exceed all other forms considered (see above), strongly suggests, that the functional form of the model is one that is most physically relevant for describing the dynamical attributes of the FPLL interaction with the pHH thin films. Diffusional exponent coefficients were calculated from these data, restricting its range to the first 60% of the kinetic data in accordance with the standard fitting protocols. These calculations gave values of n lying between 0.081 and 0.211, with an average diffusional coefficient for the film series of 0.167 ± 0.065. These values are listed in **Table 2** along with the parameters and standard errors for the modified generalized diffusion equation. The latter fits are shown graphically along with the averaged replicate experimental kinetic data for each pHH film type in **Figure 7**a, with the gray points specifying data spanning the first 60% of the rate profile. On inspection of the latter data, it is evident that the rate profile (and fits) for film type 4 are in fact quite poor, with considerable divergences being noted in the trend line developed using the array-based sampling technique. This suggests that some heterogeneity exists in samples of this class, a feature absent in the data for film types 1–3. There we note a more generalized set of trends and fits that in fact well predict the entire range of the experimental data (seen in the Figure via the extension of the fit developed using the first 60% of the data range to its full span). These same fits give values of n (≈0.2) that are smaller than would be expected for an ideal case of absorption mediated solely by the dynamics of Fickian diffusion.

In point of fact, it is evident that broader compositionally dependent trends are evidenced in these data. This is most clearly evidenced in the data shown in Figure 7b. These data illustrate two important points. First, the quantity of FPLL taken up by each pHH gel is not the same; the largest uptake is seen in films prepared from composition type 1 inks and falls markedly (threefold) across the series. This trend is clearly seen in Figure 7b (top), which shows the reduction in equilibrium fluorescence intensity seen as the M_r value for a particular film

Table 2. Characteristic kinetic fitting parameters for pHH films.

	Fitting parameters		
Film type	k	n	RSQ
pHH-1	0.2517 ± 0.0329	0.1973 ± 0.0334	0.951
pHH-2	0.1723 ± 0.0184	0.2113 ± 0.0228	0.978
pHH-3	0.1932 ± 0.0490	0.1903 ± 0.0526	0.903
pHH-4	0.3450 ± 0.0344	0.0694 ± 0.0243	0.949

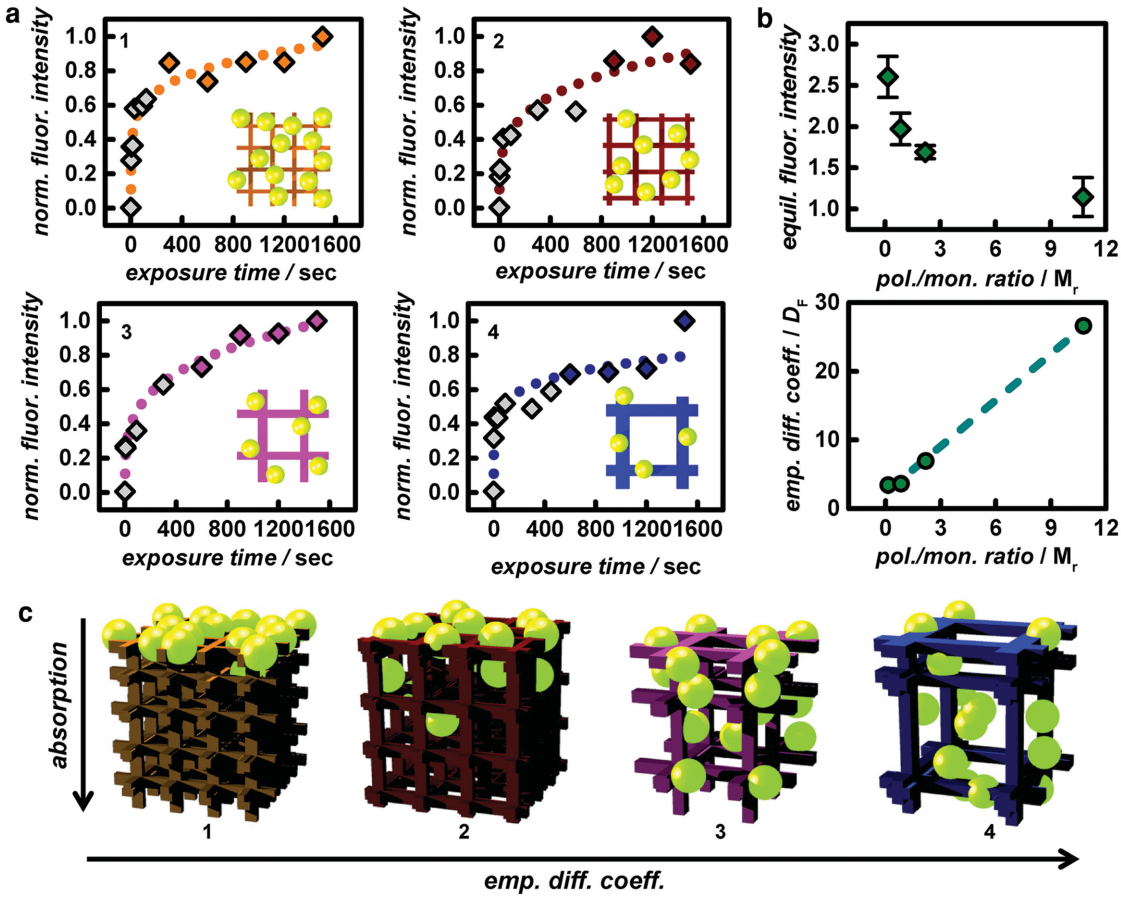

Figure 7. a) Normalized characteristic kinetic curves and Fickian fits for pHH film compositions 1–4. Gray markers correspond to data points in the first 60% of equilibration with fits shown for all pictured data points. b) Equilibrium fluorescence intensities for pHH film types 1–4 logarithmically decrease as homopolymer pHEMA content increases (top). Empirical diffusion coefficients for pHH film types 1–4 linearly correlate FPLL uptake rates with increased homopolymer content (bottom). c) Hydrogel mesh differences affect the rate of FPLL absorption kinetics, with more open mesh exhibiting faster kinetics.

type increases. High homopolymer composition inks thus yield more poorly sorptive films post-curing. The most striking effect noted is the counter trend evidenced in the rate of uptake of the FPLL by each film. To fully assess the latter aspect, we consider the quantitative attributes of the kinetics data shown, recasting it in the form of an empirical diffusion coefficient, D_F, as is discussed in the section below.

2.9. Evaluation of Empirical Diffusion Coefficients, D_F

We adopt as a starting point for an analysis of the compositional origin of the variation in FPLL uptake kinetics seen for the series of pHH hydrogel films, the calculation of an empirical diffusion coefficient equivalent, D_F, to establish the relative proficiencies of diffusing FPLL protein molecules to move throughout the gel volume. This is done using Equation (8):

$$D_F = \pi\left(\frac{h\theta}{4F_\infty}\right)^2 \quad (8)$$

where h corresponds to average film thickness (cm), and θ corresponds to the slope of the linear best fit equation for F_t/F_∞ vs. t^n.

These results are shown plotted against the M_r values for each of the pHH thin films in Figure 7b (bottom). The linear scaling evidenced (strong positive correlation coefficient of 0.996) is particularly striking. We believe this trend is best explained as arriving from a simple structural trend that follows as a result of the compositions used to prepare the inks, namely that the mesh architecture of the gel is directly impacted as a consequence of the changing densities of physical crosslinks (chain entanglements) that can be developed between the homopolymer components of the ink and the new chain formed by a propagating polymerization of the monomer constituents. An alternative model, which invokes a scaling related to relaxation dynamics of the gel appears to be strongly contradicted by the experimental values of n being significantly smaller than 1 — the latter value being of the order required for relaxation coupled transport dynamics as given in S22 (Supporting Information).[32] We conclude as a result that the distinctive molecular network mesh characteristics that result from differences in the M_r values affect not only the equilibrium mass uptake

of FPLL into the gel, but also the relative mobilities of the protein molecules throughout the polymeric mesh network as well, which is represented schematically in Figure 7c.

A useful set of structure–property correlations follows from this analysis, ones based on the inference that increasing M_r values in a pHH prepolymer solution must decrease the relative frequency with which initiation centers physically cross-link/entangle the preexisting polymer chains. These are: 1) the flexural lability of the pHEMA chains likely increases due to longer distances between points of physical cross-linking; 2) the hydrogel network mesh density is lowered by the reduced density of physical entanglements developed with the linear pHEMA chains; and 3) that the FPLL protein sorption into the gel occurs more rapidly due to the more open network mesh density that results. We believe that an entropically driven effect in the absorption of the FPLL must be operative as well. In effect the data seem to imply that the internal surface area for binding the FPLL must be reduced as a consequence of a lower density gel mesh. An important question then is why the quantity of FPLL taken up by the gel decreases more than threefold as the M_r values increase over the range explored. We believe a better physical description would be one positing enhanced osmotic repulsions leading to lower degrees of FPLL uptake within more open-mesh gels.

An important conclusion can be taken from this work, namely that fine-tuning the physicochemical properties of printable gels can be realized using simple modifications of composition without changing the underlying segmental attributes of the hydrogel chemistry, its monomer to cross-linker ratio, and without introducing gross structural perturbations (such as macroporosity) during polymerization. The results further suggest routes through which ink systems for printing scaffolds can be modified to effect specific cellular responses to bioactive molecules. For instance in the case of device implantation it may be beneficial to incorporate nonadhesive regions at certain locations to prevent fibrosis or calcification, but to induce high cellular compatibility in other regions to enable incorporation of the implant into host tissue. The current work suggests new opportunities for functional materials' design that may eventually expand to include new forms of gradient compositional/structural profiles and perhaps most importantly motifs that might be developed to carry preprogrammed temporal activity.

3. Conclusion

Model studies of the biocompatibility of PLL-treated pHH thin films and 3D scaffolds performed by culturing NIH/3T3 fibroblasts and MC-3T3-E1 preosteoblasts on these constructs show the protein treatments are essential to effect cell attachment, growth, and proliferation on these materials. Compositional differences in the inks used to print such structures in both 2D and 3D forms significantly affect cell proliferation. The modification of the pHEMA platforms, here carried out by absorption of poly-L-lysine (PLL), is essential to initiate and sustain robust forms of cell growth. This promotive effect is one that is compositionally sensitive to attributes of the ink formulation that in turn serve to impact physicochemical properties of the gel. Fibroblasts and preosteoblasts, as characterized with fluorescence microscopy and SLIM imaging, exhibit cell-specific morphologies, cytoskeletal structures, and dynamic motilities that are innate to each cell line and dictate certain attributes of their adhesion to pHH film systems. To initiate their attachment to a substrate, both cell lines rely on a high concentration of PLL absorbed into the pHH gel matrix. Most importantly, the relative quantities of attached cells appear to ultimately dictate the success of the culture. Following cellular attachment, numerous factors interact to further affect growth outcomes, including the networking dynamics on which the cells depend, the possible excess of PLL (which could over-adhere cells and reduce their networking), the modest differences in elastic modulus across the film series, and the microstructural composition of the hydrogel matrix itself. AFM mechanics characterization showed a complex spectrum of properties can be developed that are also correlated with the compositional attributes of the hydrogel inks used to prepare the HEMA substrates. In each case, attributes of physical crosslinking/entanglement (a tunable property) dominate the structure/property correlations evidenced.

Several kinetic models were considered to describe the absorption of FPLL into pHH thin films that were prepared with varying M_r ratios. It was determined that a Fickian diffusion model best described the physical system, with an average diffusional coefficient falling below the value expected for a classical case. This result arises as a consequence of the heterogeneity of the hydrogel network and its attendant mesh density. Detailed kinetics models confirm that a strong positive correlation exists between homopolymer content present in a HEMA pre-polymer ink and the resultant mobility of diffusive PLL molecules within the final (post-cure) pHH hydrogel networks. We find that, for pHH hydrogel systems, the fastest protein absorption kinetics occur in low mesh density gels, but with the consequence that this also leads to lower equilibrium protein absorption uptakes as well. The latter scaling likely reflects osmotic repulsions as mediating influences in the absorption of the PLL. From the data taken as a whole, a molecular description of the ink chemistries emerges that will be useful for the development of hydrogel ink materials for use in the construction of complex 3D printed bioscaffolds. Such materials remain areas of active study and will be reported in future publications.

4. Experimental Section

Commercially available chemical reagents were purchased from Sigma Aldrich, ATCC, Life Technologies, Polysciences Inc, and EMS Acquisition Corp. A complete reagent list is given S23 (Supporting Information). pHH solutions were prepared from pHEMA-1000, pHEMA-300, hydroxyethyl methacrylate, ethylene glycol dimethacrylate, dimethoxy-2-phenylacetophenone, ethylene glycol, ethanol, and MilliQ water then spin-cast on to clean 1.5H glass coverslips. pHH-0 and pHH-2 inks (viscous gels) were prepared by excluding ethylene glycol and ethanol from pHH-0 and pHH-2 solution compositions, and printed into 3D scaffolds with an Aerotech AGS-1000 precision custom gantry. Compositional parameters of pHH solutions, spin-casting protocols, and a detailed description of the 3D printing platform are given in S24 (Supporting Information).

AFM measurements were performed with PNP-TR SiN cantilevers purchased from NanoAndMore USA Inc. on an Asylum AFM and analyses were performed with Asylum Research Software MFP3D. Details regarding intensive replicate mechanics measurements that

yielded near-quantitative modulus data are given in S25 (Supporting Information).

NIH/3T3 embryonic murine fibroblasts and MC-3T3-E1 preosteoblasts were cultured and passaged according to the recommended protocols for each cell line. Films and scaffolds seeded with these cell cultures were fixed and stained with a standard immunofluorescent protocol or stained live with a LIVE/DEAD fluorescent assay and then imaged with a Zeiss 7 Live Confocal Fluorescence microscope or a Zeiss Axiovert 25 Fluorescence microscope for each preparation, respectively. Details regarding culture and imaging protocols are given in S26 (Supporting Information). The MTrackJ plug-in was used for the cell tracking analysis. Addition details regarding SLIM imaging methods and protocols are given in S27 (Supporting Information).[33]

The microreaction chamber used for kinetics studies was fabricated by integrating a custom-printed plate with a spin-cast pHH film coverslip on which an array of pHH film grids had been selectively patterned. The protocol for kinetics studies used rigorous replicate controls in which an aqueous solution of FPLL (0.5 mg mL^{-1}) was divided into aliquots (100 µL) and stored at –20 °C in the dark until immediately prior to use, then selectively deposited on a pHH film grid of interest. A stopwatch was used for accurate timing of FPLL incubation, which was followed by replicate rinses. A Zeiss 7 Live CFM was used for all measurements, with all settings identical for all kinetics experiments. Detailed kinetics experiment protocols as microscope settings are given in S28 (Supporting Information).

Supporting Information

Supporting Information is available from the Wiley Online Library or from the author.

Acknowledgements

The authors thank Professor Jonathan V. Sweedler, Stanislav S. Rubakhin, and Emily G. Tillmaand for their instruction and for use of their microscopy facilities. The authors also thank Julio Soares and Matthew Curtis for their helpful advice regarding confocal fluorescence microscopy. Additionally, the authors thank Scott Maclaren and Ted Limpoco for their thoughtful recommendations regarding AFM mechanics measurements as well as Lucas Osterbur for his rheological measurements. This material is based upon work supported by the Army Research Office Award No. W911NF-13-0489 through the Frederick Seitz Materials Research Laboratory at the University of Illinois at Urbana-Champaign and the Wyss Institute in the School of Engineering and Applied Sciences at Harvard University.

Received: November 3, 2015
Revised: January 28, 2016
Published online: February 29, 2016

[1] a) B. V. Slaughter, S. S. Khurshid, O. Z. Fisher, A. Khademhosseini, N. A. Peppas, *Adv. Mater.* **2009**, *21*, 3307; b) C. M. Kirschner, K. S. Anseth, *Acta Mater.* **2013**, *61*, 931; c) S. Hong, S-J. Song, J. Y. Lee, H. Jang, J. Choi, K. Sun, Y. Park, *J. Biosci. Bioeng.* **2013**, *116*, 2.

[2] a) I. C. Um, D. Fang, B. S. Hsiao, A. Okamoto, B. Chu, *Biomacromolecules* **2004**, *5*, 1428; b) A. P. Napolitano, D. M. Dean, A. J. Man, J. Youssef, D. N. Ho, A. P. Rago, M. P. Lech, J. R. Morgan, *Biotechniques* **2007**, *43*, 494; c) E. Sutanto, K. Shigeta, Y. K. Kim, P. G. Graf, D. J. Hoelzle, K. L. Barton, A. G. Alleyne, P. M. Ferreira, J. A. Rogers, *J. Micromech. Microeng.* **2012**, *22*, 045008; d) P. Zorlutuna, N. Annabi, G. Camci-Unal, M. Nikkhah, J. M. Cha, J. W. Nichol, A. Manbachi, H. Bae, S. Chen, A. Khademhosseini, *Adv. Mater.* **2012**, *24*, 1782.

[3] a) T. V. Chirila, I. J. Constable, G. J. Crawford, S. Vijavasekaran, D. E. Thompson, Y-C. Chen, W. A. Fletcher, B. J. Griffin, *Biomaterials* **1993**, *14*, 26; b) L. Shapiro, S. Cohen, *Biomaterials* **1997**, *18*, 583; c) U. J. Kim, J. Park, H. J. Kim, M. Wada, D. L. Kaplan, *Biomaterials* **2005**, *26*, 2775; d) Y. Gong, L. He, J. Li, Q. Zhou, Z. Ma, C. Gao, J. Shen, *J. Biomed. Mater. Res. Part B: Appl. Biomater.* **2006**, *82*, 192; e) J. Webber, L. Bergstrom, *Macromolecules* **2009**, *42*, 8234; f) W-C. Lai, S-C. Tseng, *Nanotechnology* **2009**, *20*, 475606; g) A. Dhanasingh, J. Salber, M. Moeller, J. Groll, *Soft Matter* **2010**, *6*, 618.

[4] a) P. Bajaj, X. Tang, T. A. Saif, R. Bashir, *J. Biomed. Mater. Res. A.* **2010**, *95A*, 1261; b) J. Lee, A. A. Abdeen, D. Zhang, K. A. Kilian, *Biomaterials* **2013**, *34*, 8140; c) A. Higuchi, Q-D. Ling, Y. Chang, S-T. Hsu, A. Umezawa, *Chem. Rev.* **2013**, *113*, 3297.

[5] a) W. Wu, C. J. Hansen, A. M. Aragón, P. H. Geubelle, S. R. White, J. A. Lewis, *Soft Matter* **2010**, *6*, 739; b) C. J. Hansen, S. R. White, N. R. Sottos, J. A. Lewis, *Adv. Funct. Mater.* **2011**, *21*, 4320; c) L. Sun, S. T. Parker, D. Syoji, X. Wang, J. A. Lewis, D. L. Kaplan, *Adv. Healthcare Mater.* **2012**, *1*, 729; d) D. B. Kolesky, R. L. Truby, A. S. Gladman, T. A. Busbee, K. A. Homan, J. A. Lewis, *Adv. Mater.* **2014**, *26*, 3124.

[6] a) B. Y. Ahn, S. B. Walker, S. C. Slimmer, A. Russo, A. Gupta, S. Kranz, E. B. Duoss, T. F. Malkowski, J. A. Lewis, *J. Vis. Exp.* **2011**, *58*, 3189; b) L. Sun, S. T. Parker, D. Syoji, X. Wang, J. A. Lewis, D. L. Kaplan, *Adv. Healthcare Mater.* **2012**, *1*, 729; c) C. J. Hansen, R. Saksena, D. B. Kolesky, J. J. Vericella, S. J. Kranz, G. P. Muldowney, K. T. Christensen, J. A. Lewis, *Adv. Mater.* **2012**, *25*, 96.

[7] J. N. Hanson Shepherd, S. T. Parker, R. F. Shepherd, M. U. Gillette, J. A. Lewis, R. G. Nuzzo, *Adv. Funct. Mater.* **2011**, *21*, 47.

[8] a) B. K. Denizli, H. K. Can, Z. M. O. Rzaev, A. Guner, *Polymer* **2004**, *45*, 6431; b) H. V. Chavda, C. N. Patel, *Indian J. Pharm. Sci.* **2011**, *73*, 30; c) J. J. Schmidt, J. H. Jeong, V. Chan, C. Cha, K. Baek, M-H. Lai, R. Bashir, H. Kong, *Biomacromolecules* **2013**, *14*, 1361; d) C. Cha, P. Soman, W. Zhu, M. Nikkhah, G. Camci-Unal, S. Chen, A. Khademhosseini, *Biomater. Sci.* **2014**, *2*, 703.

[9] R. A. Barry III, R. F. Shepherd, J. N. Hanson, R. G. Nuzzo, P. Wiltzius, J. A. Lewis, *Adv. Mater.* **2009**, *21*, 2407.

[10] a) S. H. Kim, A. Opdahl, C. Marmo, G. A. Somorjai, *Biomaterials* **2002**, *23*, 1657; b) X. M. Chen, A. C. Dunn, W. G. Sawyer, M. Sarntinoranont, *J. Biomech. Eng.-Trans. Asme* **2007**, *129*, 156; c) J. M. González-Méijome, A. López-Alemany, J. B. Almeida, M. A. Parafita, *J. Biomed. Mater. Res. Part B: Appl. Biomater.* **2008**, *88B*, 75; d) D. Passeri, M. Rossi, E. Tamburri, M. L. Terranova, *Anal. Bioanal. Chem.* **2013**, *405*, 1463.

[11] a) Z. Wang, L. Millet, M. Mir, H. Ding, S. Unarunotai, J. A. Rogers, M. U. Gillette, G. Popescu, *Opt. Express* **2011**, *19*, 1016; b) Z. Wang, L. Millet, V. Chan, H. Ding, M. U. Gillete, R. Bashir, G. Popescu, *J. Biomed. Opt.* **2011**, *16*, 026019; c) B. Bhaduri, D. Wickland, R Wang, V. Chan, R. Bashir, G. Popescu, *PLoS One* **2013**, *8*, e56930; d) M. Mir, T. Kim, A. Majumder, M. Xiang, R. Wang, S. C. Liu, M. U. Gillette, S. Stice, G. Popescu, *Sci. Rep.* **2014**, *4*, 4434.

[12] L. Wang, B. Sun, K. S. Ziemer, G. A. Barabino, R. L. Carrier, *J. Biomed. Mater. Res. Part A* **2009**, *93A*, 1260.

[13] a) C. Shan, H. Yang, D. Han, Q. Zhang, A. Ivaska, L. Niu, *Langmuir* **2009**, *25*, 12030; b) A. Grotzky, Y. Manaka, S. Fornera, M. Willeke, P. Walde, *Anal. Methods* **2010**, *2*, 1448; c) Y. Chen, W. Cao, J. Zhou, B. Pidhatika, B. Xiong, L. Huang, Q. Tian, Y. Shu, W. Wen, I.-M. Hsing, H. Wu, *ACS Appl. Mater. Interfaces* **2015**, *7*, 2919.

[14] a) K. Jo, M. L. Heien, L. B. Thompson, M. Zhong, R. G. Nuzzo, J. V. Sweedler, *Lab Chip* **2007**, *7*, 1454; b) L. J. Millet, M. E. Stewart, J. V. Sweedler, R. G. Nuzzo, M. U. Gillette, *Lab Chip* **2007**, *7*, 987; c) L. J. Millet, M. E. Stewart, R. G. Nuzzo, M. U. Gillette, *Lab Chip* **2010**, *10*, 1525.

[15] a) R. Muller, A. Eidt, K-A. Hiller, V. Katzur, M. l. Subat, H. Schweikl, S. Imazato, S. Ruhl, G. Schmalz, *Biomaterials* **2009**, *30*, 4921; b) H. Zhang, J. N. Hanson, R. G. Nuzzo, *Soft Matter* **2010**, *6*, 2238; c) A. Guan, Z. Li, K. S. Phillips, *J. Fluoresc.* **2014**, *24*, 1639.
[16] J. N. Shepherd, *Manipulating soft materials to direct cell growth in multiple dimensions (Doctoral dissertation)*, Retrieved from IDEALS database, http://hdl.handle.net/2142/15524, **2010**.
[17] C. J. Hansen, S. R. White, N. R. Sottos, J. A. Lewis, *Adv. Funct. Mater.* **2011**, *21*, 4320.
[18] S. Sridharan, M. Mir, G. Popescu, *Opt. Express* **2011**, *2*, 2815.
[19] a) V. Torres-Costa, G. Martinez-Munõz, V. Sánchez-Vaquero, Á. Muñoz-Noval, L. González-Méndez, E. Punzón-Quijorna, D. Gallach-Pérez, M. Manso-Silván, A. Climent-Font, J. P. García-Ruiz, R. J. Martín-Palma, *Int. J. Nanomed.* **2012**, *7*, 623; b) J. Wu, Z. Mao, L. Han, J. Xi, Y. Zhao, C. Gao, *J. Bioact. Compat. Polym.* **2013**, *28*, 605; c) V. Dinca, P. Alloncle, P. Delaporte, V. Ion, L. Rusen, M. Filipescu, C. Mustaciosu, C. Luculescu, M. Dinescu, *Appl. Surf. Sci.* **2015**, *352*, 82.
[20] a) J. L. Drury, D. J. Mooney, *Biomaterials* **2003**, *24*, 4337; b) W. Kim, D. C. Tretheway, S. S. Kohles, *J. Biomech.* **2009**, *42*, 395; c) N. D. Evans, C. Minelli, E. Gentleman, V. LaPointe, S. N. Patankar, M. Kallivretaki, X. Chen, C. J. Roberts, M. M. Stevens, *Eur. Cells. Mater.* **2009**, *18*, 1; d) T. A. Ulrich, A. Jain, K. Tanner, J. L. MacKay, S. Kumar, *Biomaterials* **2010**, *31*, 1875; e) J. H. Wen, L. G. Vincent, A. Fuhrmann, Y. S. Choi, K. C. Hribar, H. Taylor-Weiner, S. C. Chen, A. J. Engler, *Nat. Mater.* **2014**, *13*, 979; f) M. Goktas, G. Cinar, J. Orujalipoor, S. Ide, A. B. Tekinay, M. O. Guler, *Biomacromolecules* **2015**, *16*, 1247; g) J. Lee, A. A. Abdeen, X. Tang, T. A. Saif, K. A. Kilian, *Biomaterials* **2015**, *69*, 174.
[21] a) K. L. Johnson, *Contact Mechanics*, Cambridge University Press, Cambridge, UK **1987**, 1; b) D. C. Lin, E. K. Dimitriadis, F. Horkay, *J. Biomech. Eng.* **2007**, *129*, 430; c) P. J. Nowatzki, C. Franck, S. A. Maskarinec, G. Ravichandran, D. A. Tirrell, *Macromolecules* **2008**, *41*, 1839.
[22] a) D. Xu, K. M. Liechti, K. Ravi-Chandar, *J. Colloid Interface Sci.* **2007**, *315*, 772; b) J. F. Waters, S. Lee, P. R. Guduru, *Int. J. Solids Struct.* **2009**, *46*, 1033; c) D. S. Grierson, E. E. Flater, R. W. Carpick, *J. Adhes. Sci. Technol.* **2005**, *19*, 291.
[23] D. C. Lin, F. Horkay, *Soft Matter* **2008**, *4*, 669.
[24] D. Xu, K. M. Liechti, K. Ravi-Chandar, *J. Colloid Interface Sci.* **2007**, *315*, 772.
[25] a) C. S. Chen, M. Mrksich, S. Huang, G. M. Whitesides, D. E. Ingber, *Science* **1997**, *276*, 1425; b) Hadjipanavi, V. Mudera, R. A. Brown, *J. Tiss. Eng. Regen. Med.* **2009**, *3*, 77.
[26] J. F. Waters, S. Lee, P. R. Guduru, *Intl. J. Solids Struct.* **2009**, *46*, 1033.
[27] R. W. Glaser, *Anal. Biochem.* **1983**, *213*, 152.
[28] a) P. R. Edwards, A. Gill, D. V. Pollardknight, M. Hoare, P. E. Buckle, P. A. Lowe, R. J. Leatherbarrow, *Anal. Biochem.* **1995**, *231*, 210; b) A. W. Marczewski, *Langmuir* **2010**, *26*, 15229; c) Z. Wang, T. Yue, Y. Yuan, R. Cai, C. Niu, C. Guo, *Int. J. Biol. Macromol.* **2013**, *58*, 57.
[29] a) D. J. T. Hill, A. K. Whittaker, *Radiat. Phys. Chem.* **2011**, *80*, 213; b) P. Y. Ghi, D. J. T. Hill, D. Maillet, A. K. Whittaker, *Polym. Commun.* **1997**, *38*, 3985.
[30] N. A. Peppas, L. Brannon-Peppas, *J. Food Eng.* **1994**, *22*, 189.
[31] P. L. Ritger, N. A. Peppas, *J. Controlled Release* **1987**, *5*, 23.
[32] J. S. Vrentas, C. M. Jarzebski, J. L. Duda, *AIChE J.* **1975**, *21*, 894.
[33] E. Meijering, O. Dzyubachyk, I. Small, *Methods Enzymol.* **2012**, *504*, 183.

